

> REPLACE THIS LINE WITH YOUR MANUSCRIPT ID NUMBER (DOUBLE-CLICK HERE TO EDIT) <

Atmospheric Scattered Light Field Sampling for Improving Reconstruction Efficiency

Yihui Fan, Dongyu Du, Hongkun Cao, Jiayu Xie and Xin Jin*, *Senior Member, IEEE*

Abstract—Light field (LF) atmospheric descattering methods using multi-view images from camera arrays offer significant advantages for solving strong scattering due to their ability in exploiting high-dimensional light information. However, the relationship between performance and scattered LF sampling rate (i.e., the density of samples per unit area) is an unknown coupling, affecting acquisition and processing complexity. In this paper, we define the minimum atmospheric scattered LF sampling rate under optimal descattering quality, based on attenuated spectral support in scattering scenarios derived from the proposed atmospheric point spread function (APSF). The proposed APSF integrates the camera model, radiative transfer equation, and modified generalized Gaussian distribution (GGD) to describe multiple scattering. For any scattering parameters, the proposed APSF can be directly derived without infinite series, ensuring full adaptability to all acquisition systems through the integration of system model. Combining APSF with scene and acquisition system information, the scattered LF spectrum is determined, and consequently the minimum atmospheric scattered LF sampling rate is derived for the first time. Experimental results demonstrate the accuracy, effectiveness, and robustness of the proposed atmospheric scattered LF sampling theory through comparisons of atmospheric descattering performance across different LF sampling rates, object types, scene depths, and scattering intensities. The proposed method achieves a reduction in the number of acquisition cameras by an average of 78.4% while maintaining processing quality, which significantly enhances the applicability of LF atmospheric descattering methods.

Index Terms—light field, sampling theory, scattering imaging, computational imaging

I. INTRODUCTION

LIGHT field (LF) atmospheric descattering methods [1-11] use light intensities and angles recorded by multi-view imaging to improve the atmospheric descattering performance in strong scattering. Compared with traditional atmospheric descattering methods [12-17] that rely on two-dimensional intensity data, LF atmospheric descattering methods present higher capabilities in imaging under strong scattering scenarios [2], reducing noise for higher signal-to-noise ratios [18], extracting depth information for more accurate scattering process inversion [8], and eliminating

occlusions from scattered particles [19]. Thus, LF atmospheric descattering methods exhibit a significant advantage in enhancing scattering removal performance.

However, a major limitation of LF atmospheric descattering methods is their reliance on the LF sampling rate, defined as the density of image samples per unit area [20]. In multi-view systems used for LF atmospheric descattering, this sampling rate corresponds to the density of cameras per unit area, determining the camera spacing in the systems. For artifact-free LF reconstruction, the minimum sampling rate is calculated based on the LF spectral support without aliasing [21], which dictates the maximum camera spacing Δt_{max} in the systems. The LF spectrum is determined by the scene's depth range [21], texture complexity [22], surface reflectance [23] and occlusions [24]. In scattering scenarios, the spectrum is further attenuated by scattering media, leading to a loss of high-frequency details. Consequently, the unreasonable sampling rate often results in blurry or indistinguishable reconstructions. Increasing the LF sampling rate enhances the number of signal photons—those reflected by the target and transmitted without scattering [25]—thus improving reconstruction quality, but also raising acquisition and processing complexity. Therefore, it is essential to define an optimal minimum LF sampling rate that balances reconstruction quality and acquisition complexity in scattering scenarios.

To the best of our knowledge, no existing LF sampling theory has been explored in scattering scenarios. To fill this research gap, in this paper, we proposed a LF sampling theory in atmospheric scattering scenarios. Our theory achieves optimal scattered LF reconstruction quality and significantly improved reconstruction efficiency by determining the minimum scattered LF sampling rate. The primary contributions of this paper are:

- We propose an analytical expression of atmospheric point spread function (APSF) integrating acquisition system parameters, offering an accurate description of light propagation in scattering media. Derived from the camera model, radiative transfer equation, and a modified generalized Gaussian distribution, our APSF offers precisely represents scattering effects without relying on infinite series, making it adaptable to various scattering parameters and acquisition systems.
- We derive the LF spectrum in atmospheric scattering scenarios using the proposed APSF, which characterizes the attenuated spectral support in scattering scenarios, incorporating both scene and acquisition system information. Based on the LF spectrum, for the first time, we determine the minimum atmospheric scattered LF

This work was supported by Shenzhen Science and Technology Program under Grant No. KCXFZ20240903094301003, China. (*Corresponding author: Xin Jin*).

Yihui Fan, Dongyu Du, Jiayu xie and Xin Jin are with the Shenzhen International Graduate School, Tsinghua University, Shenzhen, 518055, China (e-mails: fyh20@mails.tsinghua.edu.cn; ddy19@mails.tsinghua.edu.cn; xjy20@tsinghua.org.cn; jin.xin@sz.tsinghua.edu.cn).

Hongkun Cao is with the Pengcheng Laboratory, Shenzhen 518000, China (e-mails: 13589389213@163.com)

This article has supplementary material provided by the authors.

> REPLACE THIS LINE WITH YOUR MANUSCRIPT ID NUMBER (DOUBLE-CLICK HERE TO EDIT) <

sampling rate. By applying this theory, the optimal atmospheric descattering quality can be achieved with minimal sampling.

- Comprehensive experiments demonstrate that the proposed APSF outperforms existing analytical expressions in terms of accuracy and robustness, and effectively establishes the minimum scattered LF sampling rate. The LF sampling theory is validated in real-world atmospheric scattering scenarios through deployment on a drone platform, enabling precise reconstruction of scattered light fields. Additionally, our approach reduces the number of acquisition cameras by 78.4% compared to current LF atmospheric descattering systems while maintaining equivalent processing quality. This reduction significantly decreases system complexity and broadens the applicability of LF atmospheric descattering technologies.

The remainder of this paper is organized as follows. Section II details the related research work in light field sampling and atmospheric descattering. Section III describes the proposed analytical expression of APSF and the proposed light field sampling in the atmospheric scattering scenarios. The experimental setup, the correctness, effectiveness and robustness of the proposed analytical expression of APSF and the proposed LF sampling theory are provided in Section IV. Conclusions are drawn in Section V.

II. RELATED WORKS

A. Light Field Atmospheric Descattering Methods

Existing light field (LF) atmospheric descattering methods [1-11] are classified into spatial domain [1-9] and frequency domain approaches [10, 11], exploiting differences in the spatial and angular distribution of scattered and ballistic light [1-9] and the epipolar-plane image (EPI) spectrum [10, 11], respectively. In spatial domain methods, photon counting uses maximum-likelihood estimation to estimate parameters of the scattering Gaussian model and remove scattering [1]. Gamma correction and histogram equalization [3], as well as color space conversion [4], are employed to enhance contrast, while statistical estimation [2] and adaptive statistical methods [5] are used to isolate ballistic photons. Additionally, guided filter [6], refocusing [7], all-in-focus imaging [8], and polarization [9] are applied to suppress scattering noise and eliminate occlusions. In frequency domain methods, object depths are estimated using grey level local variance [10], followed by the application of a hyperfan filter for adaptive atmospheric descattering [10, 11].

B. Light Field Sampling Theories

Light field sampling theories offer a systematic approach to determining optimal sampling rates across diverse scene conditions. Chai et al. [21] were the first to analyze the

spectrum of the plenoptic function, deriving the minimum LF sampling rate for Lambertian and non-occlusion scenes. They established the relationship between the Nyquist sampling rate in the LF and parameters such as the minimum and maximum object depth, camera focal length, and pixel size. This spectral analysis was extended to non-Lambertian scenes [23, 26], scenes with occlusions [24, 27], and complex textured scenes [22, 28, 29]. For non-Lambertian scenes, as an object's surface approaches perfect reflectivity, the frequency band broadens, requiring a higher LF sampling rate [26]. Using the Phong model [30], the minimum sampling rate for these scenes is derived [23]. In scenes with object occlusions, the LF spectrum segments at occlusion edges, necessitating higher sampling rates for larger occlusion areas [24]. For complex textured scenes, the LF spectrum consists of two regions; the minimum sampling rate is defined by quantizing the texture information, with increases in the maximum frequency of the texture signal leading to higher sampling rates [22, 28]. However, all these models assume straight-line light propagation, which is invalid in scattering scenarios where light undergoes multiple refractions and reflections.

C. Atmospheric Point Spread Function

To model LF propagation in fog, atmospheric point spread function (APSF) was derived from radiative transfer equation (RTE) using Legendre polynomial series [31]. APSF can be calculated by giving the optical thickness and forward scattering parameters. However, the resulting APSF, expressed as an infinite series, presents a complex mathematical expression and high computational complexity, limiting its practical applications. To remove the infinite series, Metari et al. [32] and Wang et al. [33] proposed a new APSF kernel using a generalized Gaussian distribution (GGD) approximation. Despite this improvement, their models still lack accuracy and cannot adapt to changes in the acquisition system, as they do not consider the mapping relationship between the radiation angles in the APSF and the image plane, nor the parameters of the acquisition system.

III. PROPOSED THEORY

This section details the proposed light field (LF) sampling theory in atmospheric scattering scenarios. Initially, the analytical expression of the atmospheric point spread function (APSF) integrating acquisition system is established to model light propagation in scattering media. Then, the LF spectrum in atmospheric scattering scenarios is derived based on the proposed APSF. Finally, the optimal reconstruction filter is defined, and the minimum LF sampling rate required to achieve optimal atmospheric descattering quality in atmospheric scattering scenarios is determined.

A. Proposed Analytical Expression of APSF Integrating Acquisition System Parameters

> REPLACE THIS LINE WITH YOUR MANUSCRIPT ID NUMBER (DOUBLE-CLICK HERE TO EDIT) <

The proposed analytical expression of APSF integrating acquisition system is derived based on the camera model, radiative transfer equation (RTE), and modified generalized Gaussian distribution (GGD). APSF describes the camera response for the light rays emitted from an isotropic point light source and transmitted through the atmosphere. Considering that multiple scattering predominantly occurs within a spherical region for a point light source [34], as shown in Fig. 1, the scattered light received by the image plane emanates from rays within a cone (bounded by the dashed gray line in Fig. 1). Defining the included angle of the cone as the imaging field of view (FOV), the imaging response for light at radiation angle θ modeled by RTE [35]:

$$\mu \frac{\partial I}{\partial T} + \frac{1 - \mu^2}{T} \frac{\partial I}{\partial \mu} = -I(T, \mu) + \frac{1}{4\pi} \int_0^{2\pi} \int_{-1}^1 P(\cos \alpha) I(T, \mu') d\mu' d\phi' \quad (1)$$

where I is the radiance; T is the optical thickness; α is the angle between the incident light direction (θ', ϕ') and the scattered light direction (θ, ϕ) passing through the scattering particle; $\mu = \cos \theta$ and $\mu' = \cos \theta'$; $P(\cdot)$ is the phase function [36] of the scattered particles. It can be solved by Legendre polynomial extension as [31]:

$$I(T, \mu) = \sum_{m=0}^{\infty} (g_m(T) + g_{m+1}(T)) L_m(\mu) \quad (2)$$

$$g_m(T) = I_0 e^{-\beta_m T - \alpha_m \log T}$$

$$\alpha_m = m + 1$$

$$\beta_m = \frac{2m+1}{m} (1 - q^{m-1})$$

where q is the forward scattering parameter, L_m is the Legendre polynomial of order m . Since m can be infinite, the Legendre polynomial extension solution is not easy to be calculated and applied to other models, limiting the real applications. Moreover, the omission of regarding the acquisition system compromises its accuracy in applications.

To integrate the acquisition system, the proposed APSF is defined on the image plane rather than in the radiation angle θ coordinate, thereby projecting Eq. (2) onto the image plane. With the imaging FOV taken as 0.2 degrees for the region of significant multiple scattering (verified in Supplementary Material Note 1), application of the law of sines within $\triangle OAL$ and $\triangle OBL$ yields the following derivation:

$$\frac{z}{\sin 90^\circ} = \frac{R}{\sin \frac{FOV}{2}} \quad (3)$$

$$\frac{z}{\sin(\pi - \theta)} = \frac{R}{\sin \gamma}$$

Thus, the relationship between radiation angle θ and the coordinates v on the image plane is given by:

$$\theta = \arcsin \frac{z}{R} \sin \gamma = \arcsin \frac{v}{\sin \frac{FOV}{2} \sqrt{f^2 + v^2}}, \quad (4)$$

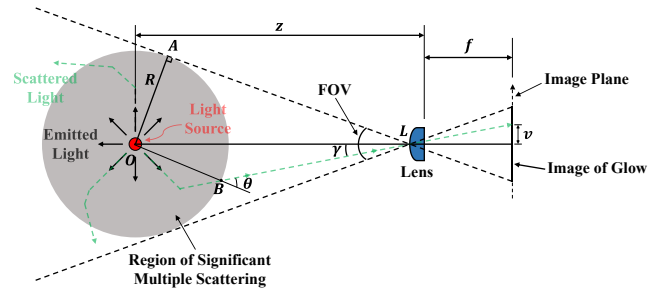


Fig. 1. Schematic diagram of APSF in multiple scattering.

where f is the camera focal length. From Eq. (4), it is evident that θ is influenced by both f and v . Given that $\tan \gamma = v/f$ and γ ranges within $[-FOV/2, FOV/2]$, $A = v/f$ spans range $[-\tan(FOV/2), \tan(FOV/2)]$. Consequently, Eq. (4) can be expressed as:

$$\theta = \arcsin \frac{A}{\sin \frac{FOV}{2} \sqrt{1 + A^2}} \quad (5)$$

Since $\mu = \cos \theta$, substituting μ into Eq. (2) yields a series of APSFs for different optical thicknesses T and forward scattering parameters q , as shown in Supplementary Material Note 2. Considering the range $[0, 1]$ of the APSF and the complexity of the scale parameters in GGD, we propose a modified GGD for more accurate description of the APSF:

$$APSF(A) = e^{-\frac{|A|^p}{\sigma}}, \quad (6)$$

where p and σ are the shape parameter and variance of APSF, respectively. In Supplementary Material Note 2, we generate a series of APSFs under various optical thicknesses T and forward scattering coefficients q , and approximate them using Eq. (6) with trust-region algorithms [37], yielding the shape parameter p and variance σ of APSF:

$$p = \left(\frac{1}{0.0014 + e^{-5T}} - \frac{1}{0.0014 + 1} \right) \times 0.005$$

$$\sigma = 0.0008 \left\{ \left[\tanh(T - 1.1) - \tanh(-1.1) \right] \times q^3 + \left[\tanh(8T - 8.8) - \tanh(-8.8) \right] \times (1 - q^3) \right\} \quad (7)$$

Substituting $A = v/f$ into Eq. (6), the proposed APSF is:

$$APSF(v) = e^{-\frac{|v|^p}{f^p \sigma}}, \quad (8)$$

and its Fourier transform is:

$$F\{APSF(v)\} = e^{-\left(\frac{\sigma f \Omega_v}{2}\right)^p}, \quad (9)$$

where $F\{\cdot\}$ denotes the Fourier transform operator, and Ω_v is the Fourier domain representation of v .

Based on the above analysis, we use RTE, camera model and modified GGD to model analytical expression of APSF integrating acquisition system, forming the foundation of the LF sampling theory in scattering scenarios.

B. Proposed Light Field Spectrum in Atmospheric Scattering Scenarios

To describe the LF in atmospheric scattering scenarios, the

> REPLACE THIS LINE WITH YOUR MANUSCRIPT ID NUMBER (DOUBLE-CLICK HERE TO EDIT) <

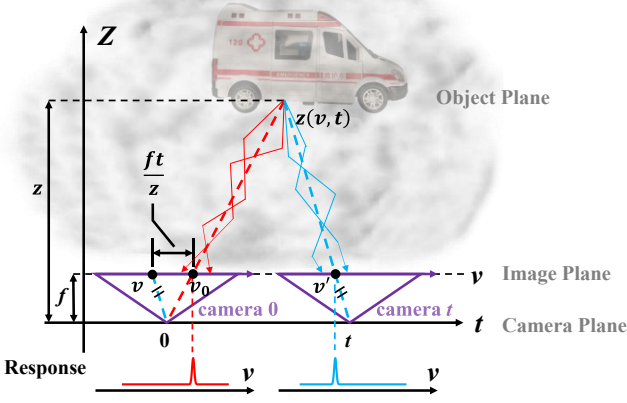


Fig. 2. Schematic diagram of the 2D light field of camera 0 and camera t observing a point in scattering scenarios.

4D light field model $l(u, v, s, t)$ is used, characterizing the light rays propagating from the image plane (u, v) to the camera plane (s, t) [21]. For simplicity, the derivation is conducted on $l(v, t)$, which can be directly extended to $l(u, s)$.

Taking the general assumption that the LF propagates by Lambertian reflections with no occlusion [21], the Fourier transform of light field $l(v, t)$ is denoted by $L(\Omega_v, \Omega_t)$. Treating the scattered images acquired by the camera at (v, t) as the convolution of non-scattered images and the proposed APSF in Eq. (9), the scattered LF in the frequency domain $L_s(\Omega_v, \Omega_t)$ is given by:

$$\begin{aligned} L_s(\Omega_v, \Omega_t) &= F\{l(v, t) * APSF(v)\} \\ &= L(\Omega_v, \Omega_t) \cdot F\{APSF(v)\} \\ &= \int_{-\infty}^{\infty} \int_{-\infty}^{\infty} l(v, t) e^{-j\Omega_v v - j\Omega_t t} dv dt \cdot e^{-\left(\frac{\sigma f \Omega_v}{2}\right)^p} \end{aligned} \quad (10)$$

where $*$ denotes the convolution operator.

Considering parallax, as shown in Fig. 2, the position of a point on the object plane differs on the image planes of cameras 0 and t , designated as v_0 and v' . Then the parallax is calculated as $v_0 - v = \frac{ft}{z}$, where f is the camera focal length and z is the object-camera distance. Thus, the LF spectrum at a constant depth z is:

$$L_s(\Omega_v, \Omega_t) = 2\pi L(\Omega_v) \delta\left(\frac{f}{z}\Omega_v - \Omega_t\right) e^{-\left(\frac{\sigma f \Omega_v}{2}\right)^p}, \quad (11)$$

where $L(\Omega_v)$ is the Fourier transform of $l(v, 0)$.

When the minimum depth z_{min} and maximum depth z_{max} of the scene are known, from Eq. (11), the LF spectral support is bounded by $\frac{f}{z_{min}}\Omega_v - \Omega_t = 0$ and $\frac{f}{z_{max}}\Omega_v - \Omega_t = 0$. The primary difference from non-scattering scenarios is the APSF term $e^{-\left(\frac{\sigma f \Omega_v}{2}\right)^p}$, which attenuates the scattered LF spectrum. Considering the pixel size Δv , Fig. 3 depicts the scattered LF spectrum (region in blue) and the optimal reconstruction filter in non-scattering scenarios (lined in red). The upper frequency bound of the optimal reconstruction filter in non-scattering scenarios equals $\frac{\pi}{\Delta v}$ and its frequency width of the optimal

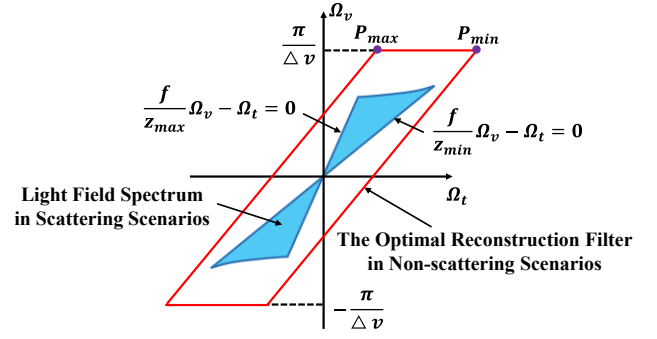


Fig. 3. Schematic diagram of the LF spectrum in scattering scenarios (region in blue) and the optimal reconstruction filter in non-scattering scenarios (lined in red).

reconstruction filter $|P_{max}P_{mix}| = \frac{\pi f}{\Delta v} \left(\frac{1}{z_{mix}} - \frac{1}{z_{max}}\right)$ determining the minimum LF sampling rate as $\Delta t_{max} = \frac{2\pi}{|P_{max}P_{mix}|}$ [21]. This frequency bound is wider than that of the scattered LF spectrum due to APSF induced attenuation. The greater the object depth z (i.e. the larger the fog's optical thickness), the greater its spectral attenuation.

This attenuation effect is verified by collecting the LF spectrum under different scattering intensities. Three color images, shown in Fig. 4(a), are placed at depth $z = 0.79\text{m}$, 0.86m , and 0.95m (representing minimum, intermediate, and maximum depth of the scene in spectral) in an artificial fog chamber (the details of the experimental system see Section IV.A). Within the optical thickness range of $T = 0$ to 2.3 , scattered LF data are captured using a moving camera array under varying scattering intensities, with each dataset comprising 179 views spaced 2 mm apart. By extracting the epipolar-plane image (EPI) from these collected data, the scattered LF spectral supports under different scattering intensities can be obtained, as shown in Fig. 4(b).

It is evident that with increasing scattering intensity (from $T = 1.2$ to 2.3), the LF spectrum is progressively attenuated due to the loss of high frequency information. This is consistent with Eq. (10), where an increase in T leads to higher values of σ and p in $e^{-\left(\frac{\sigma f \Omega_v}{2}\right)^p}$, resulting in corresponding spectrum attenuation. Therefore, a new optimal reconstruction filter needs to be designed, and the upper frequency bound on the Ω_v axis must be determined to calculate the minimum scattered LF sampling rate in scattering scenarios.

C. Proposed Optimal Reconstruction Filter and the Minimum Light Field Sampling Rate in Scattering Scenarios

$$WIDTH = \frac{4}{\sigma f} \sqrt[2]{p}. \quad (12)$$

Then, the upper frequency bound of the optimal reconstruction filter in scattering scenarios equals the maximum of $\frac{\pi}{\Delta v}$ and $\frac{WIDTH}{2}$ (the value of $WIDTH$ on the positive semi-axis) to accommodate scene complexity and the scattering effect. As objects move farther in the scene, the

> REPLACE THIS LINE WITH YOUR MANUSCRIPT ID NUMBER (DOUBLE-CLICK HERE TO EDIT) <

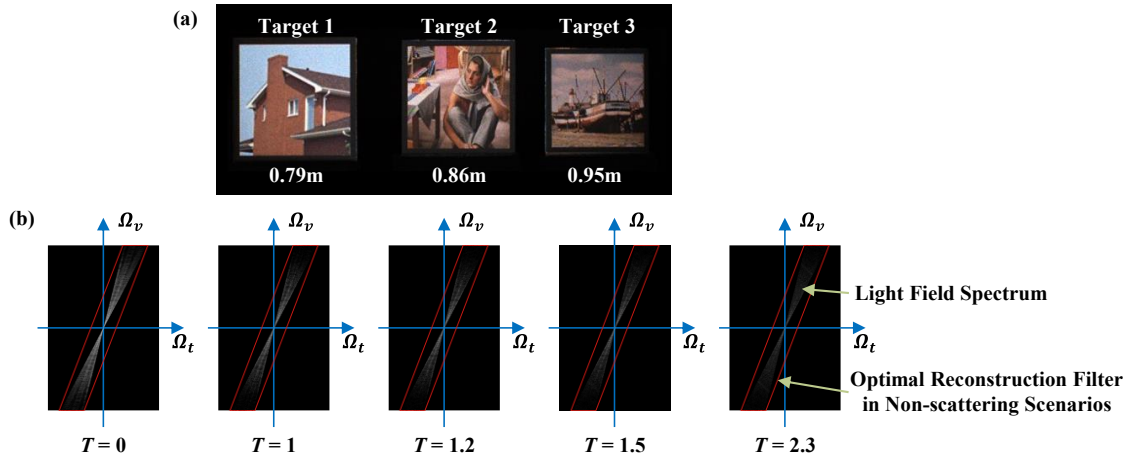


Fig. 4. Acquisition targets and LF spectrum at varying scattering intensities. (a) Depth and relative positions of targets. (b) LF spectrum (white region) attenuation at varying optical thicknesses T , and the optimal reconstruction filter in non-scattering scenarios is lined in red.

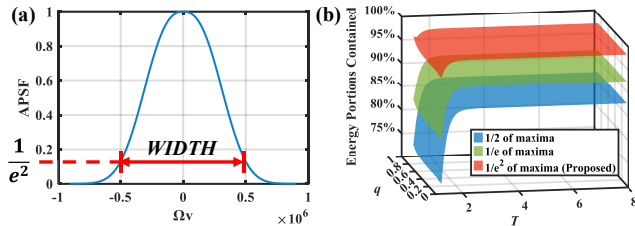


Fig. 6. (a) $WIDTH$, defined as the full width at $1/e^2$ of maxima of the proposed APSF in the frequency domain. (b) Energy portions within the full width at different intensity points of the proposed APSF at varying optical thickness in the frequency domain with the forward scattering parameter $q = 0.75$. The energy portions within the full width at $1/e^2$ of the maxima corresponds to the energy portions within the proposed $WIDTH$.

optical thickness of the scattering media increases, causing p and σ in APSF to increase, resulting in a smaller $WIDTH$ (proved in Supplementary Material Note 3). To ensure the optimal reconstruction filter works for the entire scene, $WIDTH$ calculated at the minimum object depth z_{min} , denoted as $WIDTH_{min}$, is used. Therefore, the upper frequency bound of the optimal reconstruction filter in scattering scenarios equals $\max(\frac{\pi}{\Delta v}, \frac{WIDTH_{min}}{2})$. Thus, the minimum LF sampling rate in atmospheric scattering scenarios can be derived as:

$$\Delta t_{max}^s = \frac{2\pi}{|P_{max}^s P_{mix}^s|} = \frac{2\max\left(\Delta v, \frac{2\pi}{WIDTH_{min}}\right)}{f\left(\frac{1}{z_{min}} - \frac{1}{z_{max}}\right)}, \quad (13)$$

where $|P_{max}^s P_{mix}^s| = f\left(\frac{1}{z_{mix}} - \frac{1}{z_{max}}\right) \max\left(\frac{\pi}{\Delta v}, \frac{WIDTH_{min}}{2}\right)$ corresponds to the frequency width of the scattered LF, as shown in Fig. 5.

Fig. 5 illustrates that when $\pi/\Delta v > WIDTH_{min}/2$, the upper frequency bound of the optimal reconstruction filter in scattering scenarios attenuates to $WIDTH_{min}/2$, and its

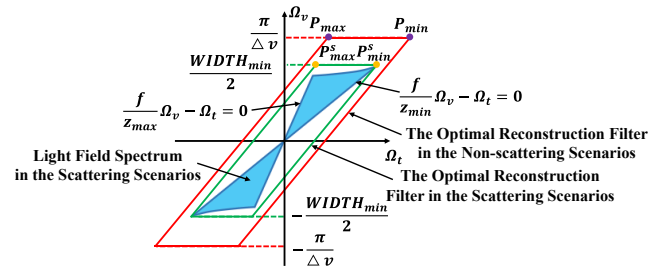


Fig. 5. Schematic of the LF spectrum in scattering scenarios (region in blue), optimal reconstruction filter in non-scattering scenarios (lined in red), optimal reconstruction filter in scattering scenarios (lined in green) and $WIDTH_{min}/2$ as the half width at $1/e^2$ of maxima of the proposed APSF in the frequency domain at depth z_{min} .

frequency width also decreases from $|P_{max} P_{mix}|$ to $|P_{max}^s P_{mix}^s|$. Using the derived minimum atmospheric scattered LF sampling rate, an optimal balance between LF acquisition/processing complexity and reconstruction quality can be achieved, as demonstrated in Section IV.D.

IV. EXPERIMENTAL RESULTS AND ANALYSIS

In this section, the correctness, effectiveness, and robustness of the proposed atmospheric scattered LF sampling theory and APSF analytical expression are demonstrated. First, the experimental setup and data acquisition are introduced. Then, the subjective and objective qualities of different APSF expressions are compared to verify the correctness of the proposed APSF. Next, $WIDTH$ values calculated by the proposed theory, existing APSF expressions, and experimental data are compared to verify the correctness and robustness of the proposed atmospheric scattered LF sampling theory and the proposed APSF. Subsequently, reconstructed scattering images at different sampling rates are evaluated to show the effectiveness and robustness of the proposed LF sampling theory in both fog chamber and real-world atmospheric scattering scenarios. Finally, the reduction in system complexity is demonstrated by comparing the

> REPLACE THIS LINE WITH YOUR MANUSCRIPT ID NUMBER (DOUBLE-CLICK HERE TO EDIT) <

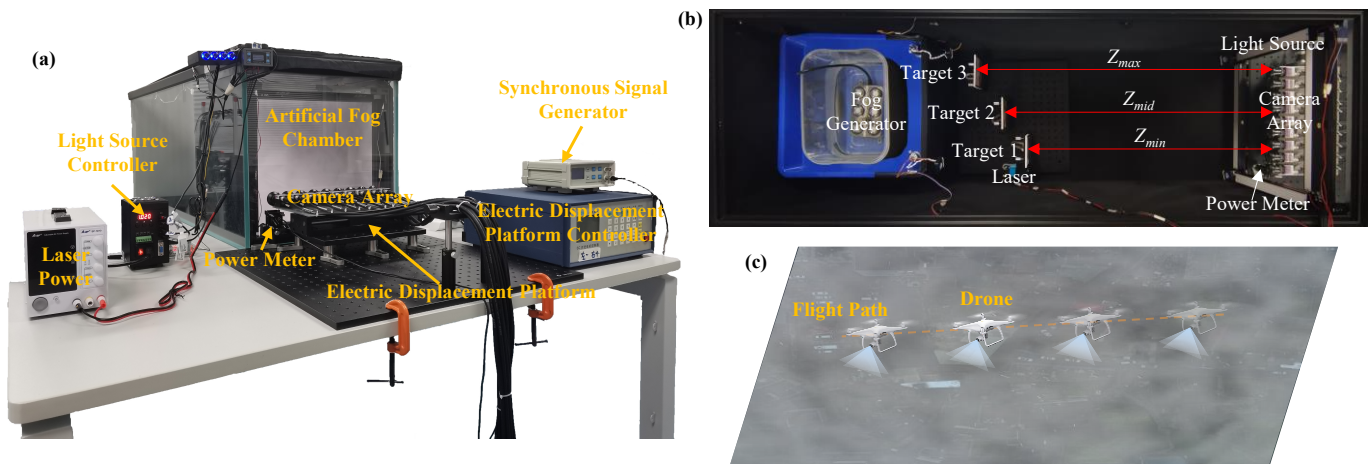


Fig. 7. Experimental setup and layout of fog scattering scenarios in both artificial fog chamber and real-world scattering scenarios. (a) Artificial fog chamber (1.5m×0.5m×0.5m) providing scattering scenarios; camera array system comprising a camera array, synchronous signal generator, electric displacement platform, and controller for LF data capture. (b) Top view of the artificial fog chamber and internal experimental setup: multi-depth targets, light source system (light sources and controllers), fogging system and optical thickness measurement system (laser and power meter). (c) An illustration of a drone flying along a predetermined path, capturing LF data in real-world atmospheric scattering scenarios.

camera spacing in actual LF atmospheric descattering systems with the spacing calculated by the proposed theory.

A. Experimental Setup and Data Acquisition

The experiments are conducted both in an artificial fog chamber and in real-world scattering scenarios, as shown in Fig. 7. The artificial fog chamber (1.5×0.5×0.5m) is lined with blackout cloth to eliminate ambient light interference, as shown in Fig. 7(a)(b). The setup includes multi-depth targets, a light source system (light sources and controller), a fogging system, an optical thickness measurement system (laser and power meter), and a camera array system (camera array, synchronous signal generator, electric displacement platform, and controller) as shown in Fig. 7(a)(b). The camera array, consisting of 9 cameras (Flir BFS-PGE-16S2; pixel size: 3.45 × 3.45 μm; image resolution: 1440 × 1080) with 4 mm lenses, mounted on an electric displacement platform to achieve dense LF acquisition through platform movement. Detailed descriptions of the experimental setup are provided in Supplementary Material Note 4. The minimum (z_{min}) and the maximum (z_{max}) scene depth are defined as the distance from the acquisition system to the nearest and farthest objects in the scene and can be directly measured. An optical thickness measurement system, consisting of a laser and a power meter, is used to determine the optical thickness T of scattering scenarios via the Beer-Lambert Law [38] (details in Supplementary Material Note 4.3). The forward scattering parameter q used in the reconstruction experiments is set to 0.75, a value widely adopted in atmospheric scattering reconstruction [31-33]. To enhance the quality of LF data acquisition, the camera array system is calibrated for both color and attitude to ensure color consistency and address translational and rotational errors between cameras, as detailed in Supplementary Material Note 5. In real-world atmospheric scattering scenarios, a drone equipped with a camera (pixel

size: 3.76 × 3.76 μm; image resolution: 5472 × 3648; focal length: 8.8 mm) is used to capture LF data, as illustrated in Fig. 7(c), details in Section IV.F.

B. Comparison of APSF Analytical Expressions

The accuracy of the proposed APSF analytical expression, which integrates acquisition system, is validated by comparison with existing models. Ground truth is generated by solving the radiative transport equation [31] within the simulation environment, which is configured with a camera featuring a 4 mm focal lens, 1440 × 1080 image resolution, and a pixel size of 3.45 × 3.45 μm. The proposed APSF is compared with the state-of-the-art models—Metari’s APSF [32], Wang’s APSF [33], Deng’s APSF[39], Tang’s APSF[40] and Zhang’s APSF [41]—under varying optical thicknesses T and forward scattering parameters q , as shown in Fig. 8. These benchmark models are widely recognized, extensively validated, and represent the latest advances in analytical APSF capable of direct image data processing. Here, the widely used typical optical thickness values ($T=1.2, 1.5, 2, 4$), representing mild to strongly dense atmospheres and effectively illustrating variations in APSF shapes, are selected for the experiments [31-33]. Additionally, forward scattering parameters $q=0.2$ (aerosols), $q=0.75$ (haze) and $q=0.9$ (fog), which represent typical weather conditions, are chosen to validate the APSF performance [31-33]. These parameter selections are widely adopted and representative in existing literature, ensuring the comparability and relevance of the results.

As illustrated in Fig. 8, the proposed APSF perform well for the different optical thicknesses T and forward scattering parameters q . small T and q (e.g., $T = 1.2$ and $q = 0.2$). However, as for comparison APSFs, as T increases (e.g., greater than 1.5), the error in Metari’s APSF increases rapidly due to not considering the mapping relationship between the radiation angles in the APSF and the image plane, as well as the parameters of the acquisition system. Wang’s APSF

> REPLACE THIS LINE WITH YOUR MANUSCRIPT ID NUMBER (DOUBLE-CLICK HERE TO EDIT) <

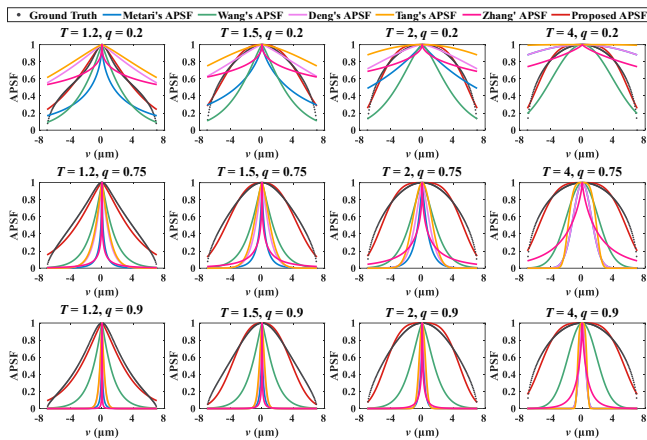


Fig. 8. Accuracy comparison of the proposed APSF under varying optical thicknesses T and forward scattering parameters q , with v representing the coordinate on the image plane.

performs better by refining the mapping between GGD parameters (p and σ) and scattering parameters (T and q) from both shape similarity and numeric reasonability. Additionally, Deng's APSF, Tang's APSF and Zhang's APSF also demonstrate subpar performance. In contrast, by establishing an accurate mapping relationship and integrating the acquisition system, the proposed APSF achieves enhanced accuracy. Furthermore, by using a modified GGD for more precise description, it demonstrates good qualitative agreement with ground truth, as shown in Fig. 8. Quantitative evaluation using Pearson linear correlation coefficient (PLCC) [42], root mean square error (RMSE) [43] and mean absolute error (MAE) [44], averaged over APSF expressions at T from 1.05 to 10 and q from 0 to 1, is presented in TABLE I. The proposed APSF achieves the highest PLCC, and the lowest RMSE and MAE, demonstrating superior correctness and robustness in modeling scattering propagation.

C. Light Field Sampling Theory and APSF in Atmospheric Scattering Scenarios

TABLE I
PERFORMANCE COMPARISON OF THE PROPOSED APSF WITH METARI'S APSF [32], WANG'S APSF [33], DENG'S APSF [39], TANG'S APSF [40] AND ZHANG'S APSF [41]

| | PLCC | RMSE | MAE |
|--------------------|---------------|---------------|---------------|
| Metari's APSF [32] | 0.7730 | 0.4046 | 0.3410 |
| Wang's APSF [33] | 0.8541 | 0.3439 | 0.2910 |
| Deng's APSF [39] | 0.7852 | 0.3910 | 0.3294 |
| Tang's APSF [40] | 0.8026 | 0.3927 | 0.3212 |
| Zhang's APSF [41] | 0.7858 | 0.6521 | 0.6170 |
| Proposed APSF | 0.9834 | 0.0504 | 0.0361 |

This experiment demonstrates the correctness and robustness of the LF sampling theory and the proposed APSF analytical expression by comparing the *WIDTH* calculated by the proposed theory, existing APSF analytical expressions and experimentally obtained data under various optical thicknesses and targets. Here, three color images (Fig. 9(a)) are placed at $z = 0.79\text{m}$, 0.86m , and 0.95m in the fog chamber. Within the optical thickness range of $T = 0$ to 2.1, scattered light field data are captured using a moving camera array under varying scattering intensities, with each dataset comprising 179 views spaced 2 mm apart.

The LF spectrum at $z_{min} = 0.79\text{m}$ in both non-scattering and scattering scenarios is extracted, and the attenuation term $e^{-(\sigma f \Omega_v / 2)^p}$ (gray dots in Fig. 9(b)) is obtained through element-wise division, with a fitted curve represents the distribution of them (blue curve in Fig. 9(b)). Comparisons of experimental *WIDTH* obtained from attenuation term and theoretical *WIDTH* are shown in Fig. 9(b). Metari's APSF [32] and Wang's APSF [33] are used to calculate the *WIDTH* for comparison by substituting the proposed APSF in the derivation of *WIDTH*, the results are shown in Fig. 9(b).

In Fig. 9(b), all *WIDTH* values align well at $T = 0.5$. As T increases to 1.2, errors in Metari's APSF *WIDTH* and Wang's APSF *WIDTH* become more significant compared to the

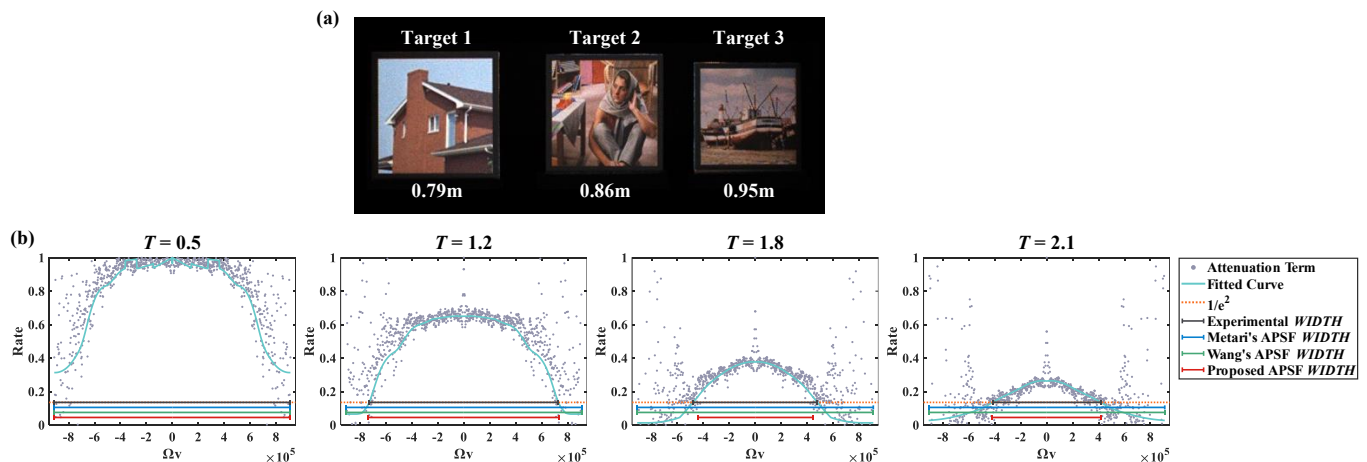


Fig. 9. Acquisition targets and attenuation term comparison. (a) Depth and relative positions of acquisition targets. (b) Attenuation term at z_{min} and its experimental *WIDTH* compared with Metari's APSF *WIDTH*, Wang's APSF *WIDTH* and proposed APSF *WIDTH* at different optical thicknesses for three color image targets.

> REPLACE THIS LINE WITH YOUR MANUSCRIPT ID NUMBER (DOUBLE-CLICK HERE TO EDIT) <

proposed APSF *WIDTH*. As scattering intensity T increases to 2.1, the experimental *WIDTH* decreases, with the proposed APSF *WIDTH* remains accurate and consistent with the experimental results, unlike the erroneous values from Metari's APSF *WIDTH* and Wang's APSF *WIDTH*. Although Wang's APSF refines the mapping between GGD parameters and scattering parameters by considering both shape similarity and numeric reasonability, along with Metari's APSF, it still fails to establish an accurate mapping relationship and does not consider the acquisition system. Benefiting from this mapping and integrating acquisition system parameters, the proposed APSF accurately describes the attenuation of the LF spectrum in atmospheric scattering scenarios, with an average error of only 1.5%. This experiment confirms the correctness of the proposed LF sampling theory and APSF expression under different optical thicknesses. Additionally, robustness is verified using complex 3D objects, with accurate results still obtained (details in Supplementary Material Note 6).

D. Minimum Light Field Sampling Rate and Atmospheric Descattering Results in Fog Chamber

In this experiment, the effectiveness and robustness of the LF sampling theory are evaluated by comparing atmospheric descattering performance using representative LF atmospheric descattering methods at various sampling rates under different objects, scene depths, and scattering intensities. Three color images are placed at $z = 0.79\text{m}$, 0.86m , and 0.95m in the fog chamber (Fig. 10(a)). Scattered LF data are captured using a moving camera array under varying scattering intensities, within the optical thickness T at 0.79m ranging from 1.2 to 4, with each dataset comprising 179 views spaced 2 mm apart. These captured views are used to construct LFs with varying sampling rates. Three representative LF atmospheric descattering methods are applied—volumetric focus [11] in the frequency domain, Peplography [2], and LFI [7] in the spatial domain—to Targets 1, 2, and 3, respectively. In this experiment, Peplography, a photon-counting-based method, has its window size for estimating the scattering media set to 150×150 pixels and an expected ballistic photon count of 50,000 for reconstruction. The LFI approach is based on refocusing techniques, enhancing the target signal at the given depth and weakening the scattering effects at other depths to achieve atmospheric descattering. The volumetric focus method uses hyperfan filtering across the 4D light field data to effectively eliminate scattering components beyond the target reconstruction depth, thereby reinforcing the desired signals within the reconstruction depth range. Consequently, we set the target depths of $z = 0.79\text{m}$, 0.86m , and 0.95m as the reconstruction depths for these three methods to reconstruct the targets. The reconstruction results at various camera spacings (i.e., distances between viewpoints, which equivalent to the sampling rates) are shown in Fig. 10(b)-(d). Quantitative indicators, cross correlation [45], structural similarity (SSIM) [46] and peak signal-to-noise ratio (PSNR) [46], are calculated to compare the reconstruction results. Cross correlation measures the degree of linear alignment between two images, offering a complementary perspective on their performance.

SSIM evaluates the structural similarity, which is crucial for assessing perceptual quality. Meanwhile, PSNR reflects the ratio between the maximum possible signal and the noise. The inflection point of the curve is identified as the experimental minimum LF sampling rate. Comparisons of the proposed and experimental minimum LF sampling rates are shown in Fig. 10(e)-(g), and for different scattering intensities in Fig. 11.

From the volumetric focus reconstruction results in Fig. 10(b), it is observed that when the spacing is 8 mm and 18 mm—exceeding the proposed minimum LF sampling rate—the house outline is sharp and aliasing-free. However, at spacings of 24mm and 30mm, aliasing stripes appear due to insufficient sampling. Fig. 10(e) reveals an inflection point where image quality significantly deteriorates as camera spacing increases and sampling rate decreases, aligning well with the proposed minimum LF sampling rate. Similarly, Peplography and LFI results in Fig. 10(c) and (d) show clear reconstructions above the proposed minimum LF sampling rate while blurriness and aliasing occur below it. Fig. 10(f) and (g) further confirm that the proposed sampling rate aligns well with experimental results across different methods and distances. Benefitting from accurate modeling of the LF in scattering scenarios based on the proposed APSF analytical expression, these results indicate the effectiveness of the LF sampling theory in different LF atmospheric descattering methods.

In Fig. 11, the robustness of the proposed theory is demonstrated across varying optical thicknesses. Building upon typical optical thickness values, we extended the range by adding additional optical thicknesses T and conducted experiments within $T=1.2$ to 4. Fig. 11(a) shows that the proposed and experimental minimum LF sampling rates for volumetric focus reconstruction of Target 1 are consistent at optical thicknesses $T=1.2$ and 2. Fig. 11(b) and (c) present similar correspondences for Peplography on Target 2 and LFI on Target 3 at optical thicknesses $T=1.5$ and 4, and $T=3$ and 3.5, respectively. These results confirm the robustness of the proposed LF sampling theory across various reconstruction methods and optical thicknesses.

To further demonstrate the robustness of the proposed theory, additional experiments are conducted on 3D targets and more complex 3D metal targets, as shown in Fig. 12 and Fig. 13, respectively. In Fig. 12, it is clearly shown that the proposed and experimental minimum light field sampling rates align consistently across different reconstructions, even for 3D targets. For the more complex 3D metal targets presented in Fig. 13, the proposed theory remains accurate despite increased complexity and the presence of reflections. Furthermore, the scene depth range is varied in Fig. 14, and the results also confirm the validity of the proposed minimum light field sampling rates. These results illustrate the strong robustness and wide applicability of the proposed theory.

E. Comparisons of LF descattering method guided by the proposed atmospheric scattered LF sampling theory and traditional single-image methods

To demonstrate the superior performance of the LF descattering method, we conduct a comparative analysis with

> REPLACE THIS LINE WITH YOUR MANUSCRIPT ID NUMBER (DOUBLE-CLICK HERE TO EDIT) <

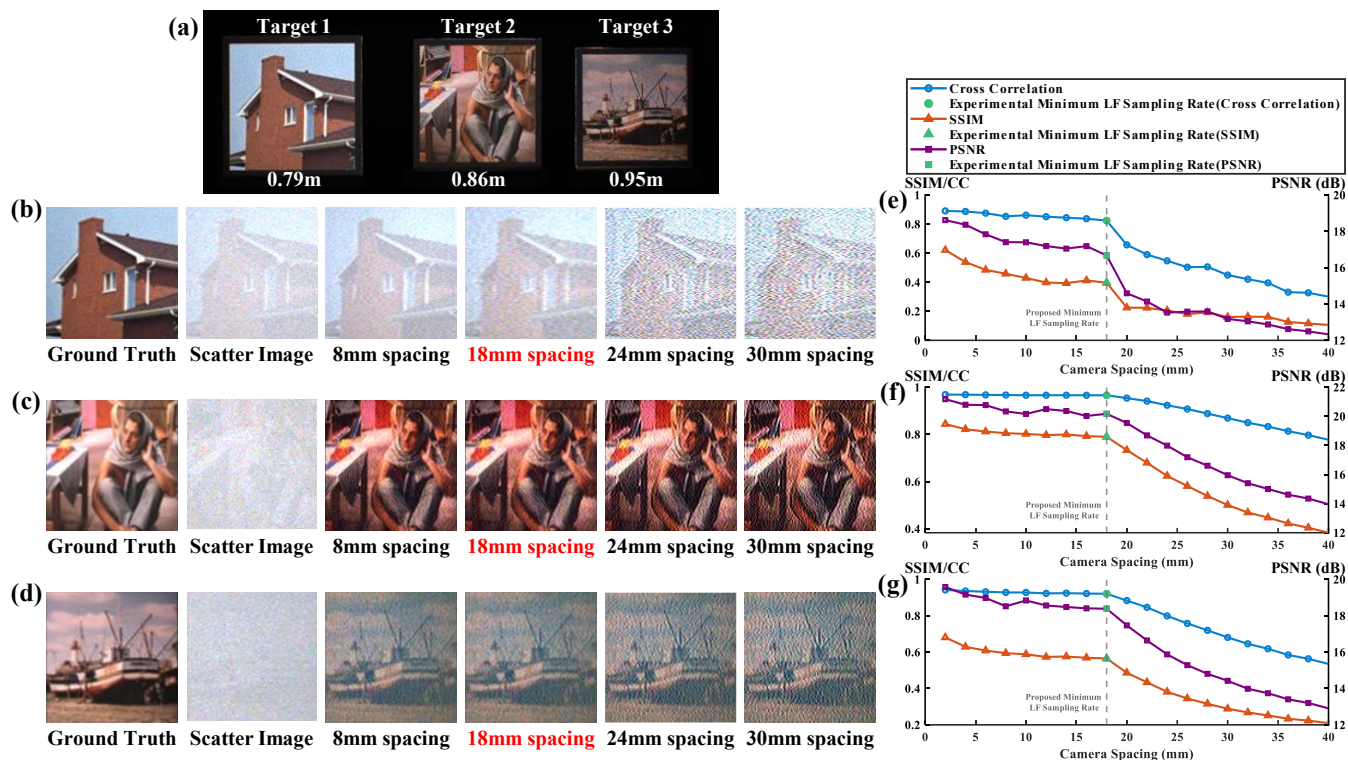


Fig. 10. Acquisition targets and reconstruction results at different sampling rates. (a) Depth and relative positions of acquisition targets. (b)-(d) Reconstruction results for Target 1, Target 2, and Target 3 using volumetric focus, Pelpography, and LFI, respectively, at varying camera spacings (i.e., distances between viewpoints, which equivalent to the sampling rates) when $T = 2.3$. (e)-(g) Cross-correlation (CC), SSIM and PSNR of reconstruction results for Target 1, Target 2, and Target 3 using volumetric focus, Pelpography, and LFI, respectively, at varying sampling rates when $T = 2.3$, including the proposed and experimentally minimum LF sampling rate.

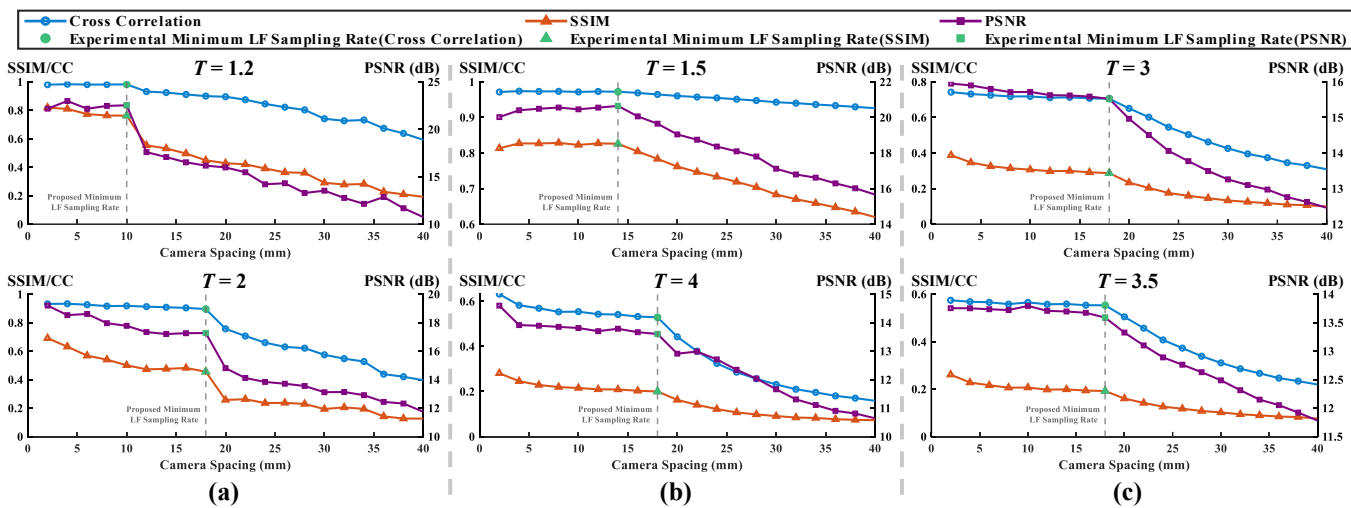


Fig. 11. Cross-correlation (CC), SSIM, and PSNR of reconstruction results. (a) Quantitative metrics of volumetric focus reconstruction for Target 1 at varying sampling rates. (b) Quantitative metrics of Pelpography reconstruction for Target 2 at varying sampling rates. (c) Quantitative metrics of LFI reconstruction for Target 3 at varying sampling rates.

traditional single-image descattering methods. The target is positioned at $z = 0.86\text{m}$ within a fog chamber (Fig. 15), and scattered images are captured at varying optical thicknesses T at 0.79m ranging from 1.8 to 3, with each dataset comprising 179 views spaced 2 mm apart. The conventional single-image descattering methods, SLP [16], UNTV [17] and

DeScatteringNN [47], serve as comparison methods to reconstruct the scattered image, while the proposed atmospheric scattered LF sampling theory guides Pelpography in the LF descattering process. The reconstructed images, along with their corresponding cross-correlation, SSIM and PSNR values, are shown in Fig. 15.

> REPLACE THIS LINE WITH YOUR MANUSCRIPT ID NUMBER (DOUBLE-CLICK HERE TO EDIT) <

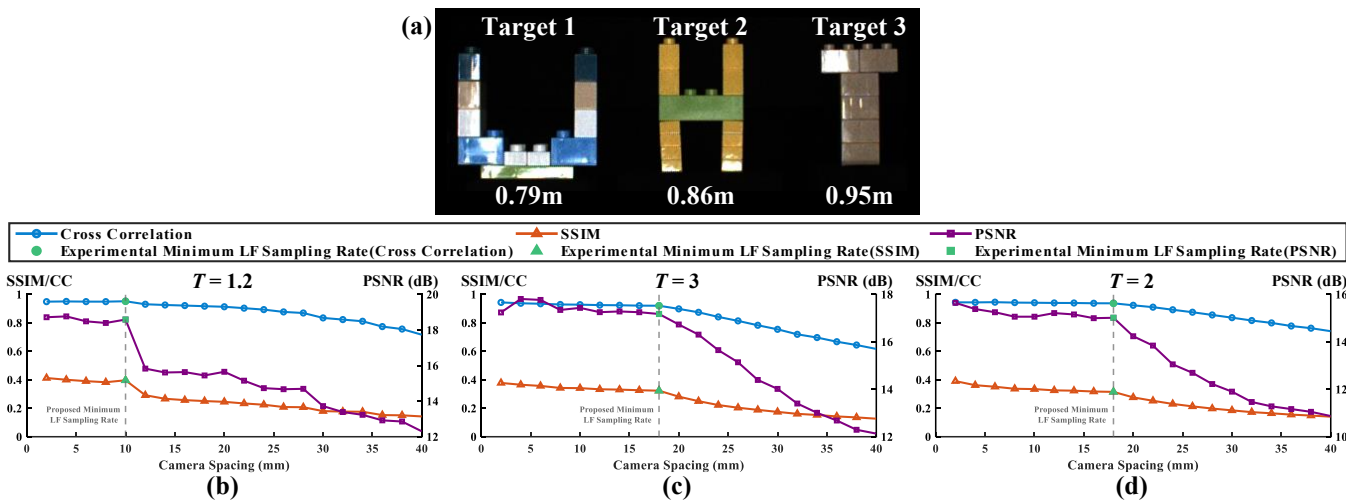


Fig. 12. Acquisition 3D targets and reconstruction metrics. (a) Depth and relative positions of targets. (b-d) Cross-correlation (CC), SSIM, and PSNR for volumetric focus (Target 1), Peplography (Target 2), and LFI (Target 3) reconstructions at varying sampling rates, respectively.

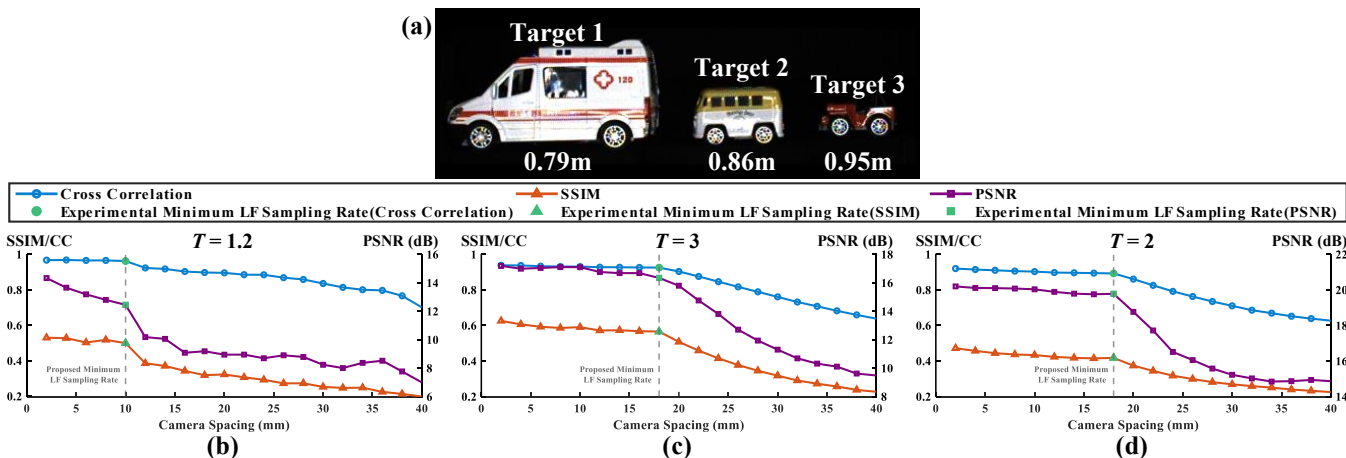


Fig. 13. Acquisition complex 3D metal targets and reconstruction metrics. (a) Depth and relative positions of targets. (b-d) Cross-correlation (CC), SSIM, and PSNR for volumetric focus (Target 1), Peplography (Target 2), and LFI (Target 3) reconstructions at varying sampling rates, respectively.

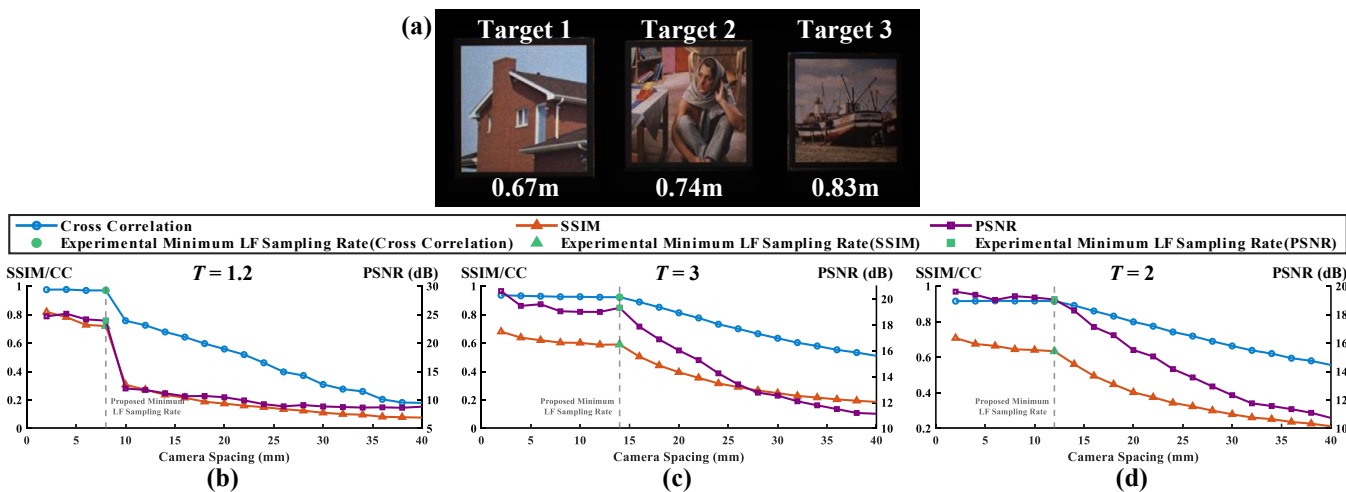


Fig. 14. Acquisition targets at different scene depth and reconstruction metrics. (a) Depth and relative positions of targets. (b-d) Cross-correlation (CC), SSIM, and PSNR for volumetric focus (Target 1), Peplography (Target 2), and LFI (Target 3) reconstructions at varying sampling rates, respectively.

> REPLACE THIS LINE WITH YOUR MANUSCRIPT ID NUMBER (DOUBLE-CLICK HERE TO EDIT) <

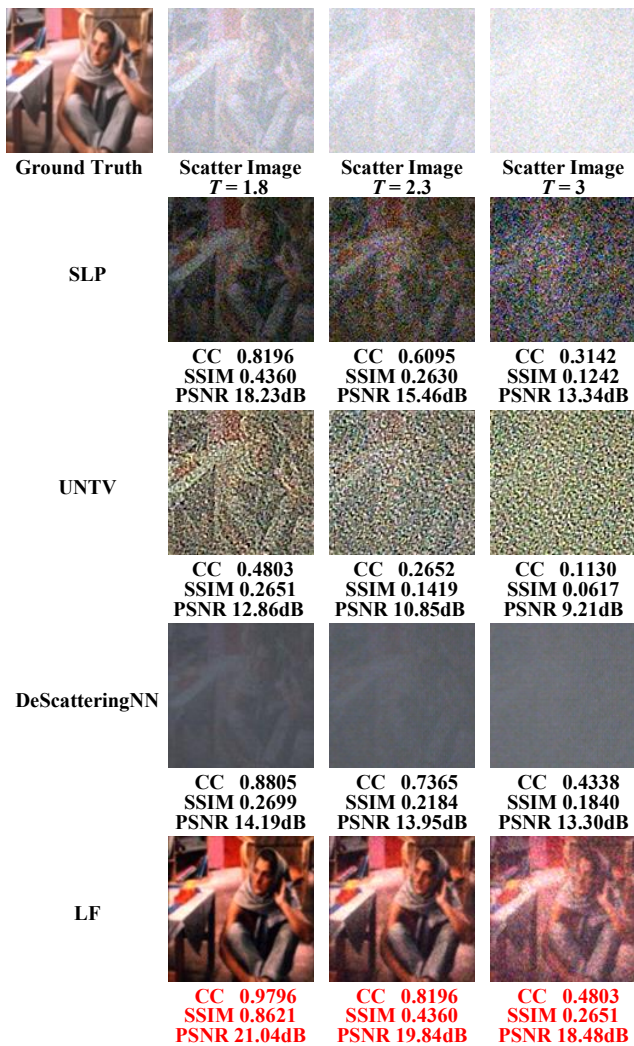


Fig. 15. Visual comparison of descattering methods between traditional single-image descattering methods (SLP [16], UNTV [17] and DeScatteringNN [47]) and light field descattering method under varying optical thickness T , with cross-correlation (CC), SSIM and PSNR metrics displayed beneath each reconstruction.

As shown in Fig. 15, SLP, UNTV and DeScatteringNN exhibit limited effectiveness in mitigating scattering effects, particularly as the optical thickness increases. The reconstructions produced by these methods suffer from significant noise and a loss of fine details, resulting in lower cross-correlation, SSIM and PSNR scores. Notably, when optical thickness T reaches 3, SLP, UNTV and DeScatteringNN fail to adequately reconstruct the target image, highlighting their limitations under severe scattering conditions. In contrast, the LF descattering method consistently outperforms these traditional techniques, delivering reconstructions with enhanced detail preservation, sharper edges, and greater fidelity to the ground truth. This is reflected in the higher cross-correlation, SSIM and PSNR values across all levels of optical thickness, underscoring the robustness and effectiveness of the LF method in maintaining image integrity in challenging scattering environments. These

results position the LF descattering method as a promising solution for high-fidelity descattering applications.

F. Minimum Light Field Sampling Rate and Atmospheric Descattering Results in Real-world Atmospheric Scattering Scenarios

The theory's effectiveness and robustness are evaluated in real-world scattering scenarios. A drone with a camera (pixel size: $3.76 \times 3.76 \mu\text{m}$; image resolution: 5472×3648 ; focal length: 8.8 mm) captured LF data, as shown in Fig. 16(a). 11 views (Fig. 16(b) and Fig. 16(c)) and 9 views (Fig. 16(d) and Fig. 16(e)), each separated by 4.1 m, are captured from real-world atmospheric scattering scenarios. The scattering intensities, estimated from the captured scatter images using the Chinese National Standard Specifications for Surface Meteorological Observation—Meteorological Visibility (GB/T 35223-2017) [48], are $T = 4.9, 3.94, 4.24, \text{ and } 4.58$, respectively. The forward scattering parameter q used in the experiments is set to 0.75, a value widely adopted in atmospheric scattering reconstruction [31-33]. The corresponding scene depth, ranging from 140m (z_{min}) to 150m (z_{max}), is obtained using drone positioning data and visual ranging techniques. LFI is used for reconstruction, and dehazing quality index (DHQI) [49] is calculated to evaluate the results (Fig. 16(b)-(e)).

The reconstruction results in Fig. 16(b) confirm that high-quality reconstructions are achieved when the sampling rate above the proposed minimum sampling rate, with no detail loss. However, as camera spacing increases, leading to a sampling rate drop below the proposed rate, high-frequency aliasing degrades image quality. Besides, the DHQI evaluation reveals a significant inflection point at a camera spacing of 8.2 m, indicating a strong correspondence between the experimental data and the proposed minimum LF sampling rates. Moreover, the test results from other scenarios (Fig. 16(c)-(e)) show similar trends, further demonstrating the effectiveness and robustness of the proposed LF sampling theory. This demonstrates the effectiveness and robustness of the proposed LF sampling theory even in complex real-world atmospheric scattering scenarios, achieving high-quality reconstruction at the proposed minimum sampling rate and enhancing reconstruction efficiency.

G. Comparison of Actual Light Field Atmospheric Descattering Systems

The role of LF sampling theory in reducing system complexity is discussed by comparing camera spacing in existing LF atmospheric descattering systems with that calculated using the proposed theory. TABLE II presents the parameters of existing LF atmospheric descattering systems and the calculated camera spacings using the proposed theory, as well as Metari's APSF [32], Wang's APSF [33], Deng's APSF [39], Tang's APSF [40] and Zhang's APSF [41] for comparison.

TABLE II demonstrates that Metari's, Wang's, Deng's, Tang's and Zhang's APSF models underperform with minimal spacing in all scenarios, while the proposed model achieves

> REPLACE THIS LINE WITH YOUR MANUSCRIPT ID NUMBER (DOUBLE-CLICK HERE TO EDIT) <

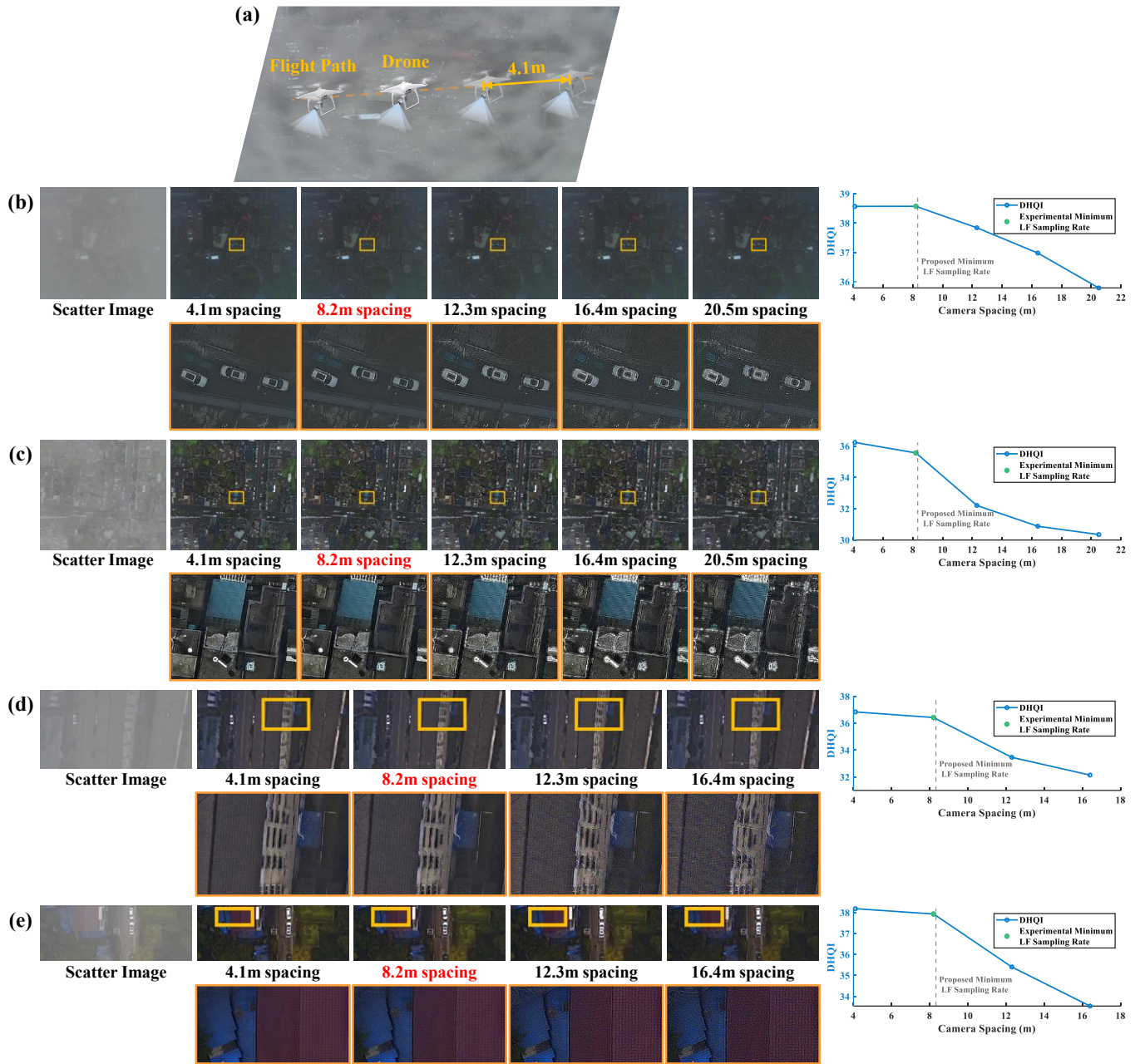


Fig. 16. Acquisition targets and reconstruction results in real-world atmospheric scattering scenarios at varying sampling rates. (a) An illustration of a drone flying along a predetermined path, capturing LF data in real-world scattering scenarios. (b-e) LFI reconstruction of scattered LF data at varying sampling rates, with corresponding DHQI values, including the proposed and experimentally determined minimum LF sampling rates.

TABLE II

Parameters of Existing LF Atmospheric Descattering Systems and Comparative Analysis of Camera Spacing in LF Atmospheric Descattering Systems Based on Existing APSF Analytical Models and Proposed LF Sampling Theory

| System | f | Δv | z_{min} | z_{max} | T | q | Δt | Metari's APSF Δt [32] | Wang's APSF Δt [33] | Deng's APSF Δt [39] | Tang's APSF Δt [40] | Zhang's APSF Δt [41] | Proposed Δt |
|---------------|-------|--------------|-----------|-----------|------|-------|------------|-------------------------------|-----------------------------|-----------------------------|-----------------------------|------------------------------|---------------------|
| System 1 [3] | 5mm | 16.2 μ m | 0.49m | 0.769m | 3.78 | 0.715 | 5mm | 0.89mm | 0.89mm | 0.89mm | 0.89mm | 0.89mm | 5.37mm |
| System 2 [4] | 6mm | 2.2 μ m | 0.35m | 0.5m | 5.2 | 0.83 | 5mm | 0.86mm | 0.86mm | 0.86mm | 0.86mm | 0.86mm | 4.55mm |
| System 3 [50] | 52mm | 4.9 μ m | 0.368m | 0.42m | 3.76 | 0.715 | 5mm | 0.55mm | 0.55mm | 0.55mm | 0.55mm | 0.55mm | 11.7mm |
| System 4 [5] | 105mm | 3.85 μ m | 0.109m | 0.116m | 2.17 | 0.715 | 2mm | 0.12mm | 0.12mm | 0.12mm | 0.12mm | 0.12mm | 6.44mm |
| System 5 [2] | 50mm | 3.85 μ m | 0.109m | 0.116m | 2.17 | 0.715 | 2mm | 0.26mm | 0.26mm | 0.26mm | 0.26mm | 0.26mm | 6.44mm |

> REPLACE THIS LINE WITH YOUR MANUSCRIPT ID NUMBER (DOUBLE-CLICK HERE TO EDIT) <

maximal spacing in most cases, indicating the least sampling requirement. This superiority is attributed to its precise modeling of the scattered LF and the seamless integration with the acquisition system. On average, the proposed model requires 24.77 times less camera usage compared to the comparison APSF models, saving 95.4% of cameras in one dimension and 99.8% in two dimensions, without sacrificing quality. Compared to existing systems, it saves 53.5% in one dimension and 78.4% in two dimensions, highlighting its benefit for LF atmospheric descattering applications.

V. CONCLUSION

In this paper, a theory for the minimum light field (LF) sampling rate in scattering scenarios is derived from the proposed atmospheric point spread function (APSF) analytical expression. This theory is aimed at achieving optimal atmospheric descattering quality at the minimum LF sampling rate. The proposed APSF incorporates the camera model, radiative transfer equation, and modified generalized Gaussian distribution (GGD) to effectively characterize multiple scattering. It allows direct derivation for any scattering parameters without infinite series, ensuring comprehensive adaptability to various acquisition systems through the integration of the system model, and offers greater accuracy compared to existing analytical expressions. The minimum LF sampling rate in atmospheric scattering scenarios is determined from the LF spectrum, which combines the proposed APSF with scene and acquisition system information. By employing this theory, the optimal atmospheric descattering quality can be achieved with minimal sampling. Experimental results across various object types, scene depths, and scattering intensities confirm the correctness, effectiveness, and robustness of the proposed LF sampling theory. Additionally, its applicability in real-world atmospheric scattering scenarios is validated. Moreover, it can save an average of 78.4% of the acquisition cameras at the same processing quality. This work provides a framework for capturing LF data in scattering environments, significantly enhancing the application of LF atmospheric descattering methods.

Although the proposed APSF performs effectively in most atmospheric scattering scenarios, it still encounters certain limitations. Specifically, when processing images with strong scattering, two major challenges arise: (a) the target signal is obscured by scattering noise, making it difficult for the detector to capture; (b) strong scattering results in amplified image noise. These challenges significantly impact the performance of APSF, which is one of the issues to address in future work.

REFERENCES

- [1] B. Tavakoli, B. Javidi, and E. Watson, "Three dimensional visualization by photon counting computational integral imaging," *Optics express*, vol. 16, no. 7, pp. 4426-4436, 2008.
- [2] M. Cho and B. Javidi, "Peplography—a passive 3D photon counting imaging through scattering media," *Optics letters*, vol. 41, no. 22, pp. 5401-5404, 2016.
- [3] M. Cho and B. Javidi, "Three-dimensional visualization of objects in turbid water using integral imaging," *Journal of display technology*, vol. 6, no. 10, pp. 544-547, 2010.
- [4] S. Komatsu and B. Javidi, "Three-dimensional Integral Imaging Visualization in Scattering Medium with Bayesian Estimation," in *17th Workshop on Information Optics*, 2018: IEEE, pp. 1-3.
- [5] M. Cho and B. Javidi, "Optical 3D visualization under inclement weather conditions," in *Three-Dimensional Imaging, Visualization, and Display*, 2018, vol. 10666: SPIE, pp. 69-80.
- [6] K. A. Skinner and M. Johnson-Roberson, "Underwater image dehazing with a light field camera," in *IEEE Conference on Computer Vision and Pattern Recognition Workshops*, 2017: IEEE, pp. 62-69.
- [7] F. Ouyang, J. Yu, H. Liu, Z. Ma, and X. Yu, "Underwater imaging system based on light field technology," *IEEE Sensors Journal*, vol. 21, no. 12, pp. 13753-13760, 2021.
- [8] J. Tian, Z. Murez, T. Cui, Z. Zhang, D. Kriegman, and R. Ramamoorthi, "Depth and image restoration from light field in a scattering medium," in *the IEEE International Conference on Computer Vision*, 2017: IEEE, pp. 2401-2410.
- [9] Y. Tian, B. Liu, X. Su, L. Wang, and K. Li, "Underwater imaging based on LF and polarization," *IEEE Photonics Journal*, vol. 11, no. 1, pp. 1-9, 2019.
- [10] V. Varghese, M. Bryson, O. Pizarro, S. B. Williams, and D. G. Dansereau, "Light Field Image Restoration for Vision in Scattering Media," in *25th IEEE International Conference on Image Processing*, 2018: IEEE, pp. 1093-1097.
- [11] D. G. Dansereau, O. Pizarro, and S. B. Williams, "Linear Volumetric Focus for Light Field Cameras," *ACM Trans. Graph.*, vol. 34, no. 2, pp. 1-20, 2015.
- [12] S. C. Agrawal and A. S. Jalal, "Dense haze removal by nonlinear transformation," *IEEE Transactions on Circuits and Systems for Video Technology*, vol. 32, no. 2, pp. 593-607, 2021.
- [13] K. He, J. Sun, and X. Tang, "Single image haze removal using dark channel prior," *IEEE transactions on pattern analysis and machine intelligence*, vol. 33, no. 12, pp. 2341-2353, 2011.
- [14] Y. Liu, Z. Yan, J. Tan, and Y. Li, "Multi-purpose oriented single nighttime image haze removal based on unified variational retinex model," *IEEE Transactions on Circuits and Systems for Video Technology*, vol. 33, no. 4, pp. 1643-1657, 2022.
- [15] D. Berman, T. Treibitz, and S. Avidan, "Single image dehazing using haze-lines," *IEEE transactions on pattern analysis and machine intelligence*, vol. 42, no. 3, pp. 720-734, 2020.
- [16] P. Ling, H. Chen, X. Tan, Y. Jin, and E. Chen, "Single image dehazing using saturation line prior," *IEEE Transactions on Image Processing*, vol. 32, no. 1, pp. 3238-3253, 2023.
- [17] J. Xie, G. Hou, G. Wang, and Z. Pan, "A variational framework for underwater image dehazing and deblurring," *IEEE Transactions on Circuits and Systems for Video Technology*, vol. 32, no. 6, pp. 3514-3526, 2021.
- [18] R. Prevedel *et al.*, "Simultaneous whole-animal 3D imaging of neuronal activity using light-field microscopy," *Nature methods*, vol. 11, no. 7, pp. 727-730, 2014.
- [19] G. Krishnan, S. Goswami, R. Joshi, and B. Javidi, "Three-dimensional integral imaging-based image descattering and recovery using physics informed unsupervised CycleGAN," *Optics Express*, vol. 32, no. 2, pp. 1825-1835, 2024.
- [20] C. Zhang and T. Chen, "Light field sampling," *Synthesis lectures on image, video, and multimedia processing*, vol. 2, no. 1, pp. 1-102, 2006.
- [21] J. Chai, X. Tong, S. Chan, and H. Shum, "Plenoptic sampling," in *the 27th annual conference on Computer graphics and interactive techniques*, 2000: ACM, pp. 307-318.
- [22] C. Zhu, H. Zhang, Q. Liu, Y. Yu, and H. Su, "Frequency analysis of light field sampling for texture information," *Optics Express*, vol. 28, no. 8, pp. 11548-11572, 2020.
- [23] P. Zhou, L. Yu, and C. Pak, "The spectrum broadening in the plenoptic function," in *International Conference on Internet Multimedia Computing and Service*, 2014: ACM, pp. 130-135.
- [24] C. Zhu, H. Zhang, and L. Yu, "An occlusion model for improving rendering quality of view," in *IEEE International Conference on Image Processing*, 2017: IEEE, pp. 2005-2009.
- [25] D. Du *et al.*, "A boundary migration model for imaging within volumetric scattering media," *Nature Communications*, vol. 13, no. 1, pp. 1-10, 2022.

> REPLACE THIS LINE WITH YOUR MANUSCRIPT ID NUMBER (DOUBLE-CLICK HERE TO EDIT) <

- [26] P. Zhou, L. Yu, and G. Zhong, "The non-Lambertian reflection in plenoptic sampling," in *IEEE International Conference on Image Processing*, 2013: IEEE, pp. 2154-2157.
- [27] C. Zhang and T. Chen, "Spectral analysis for sampling image-based rendering data," *IEEE Transactions on Circuits and Systems for Video Technology*, vol. 13, no. 11, pp. 1038-1050, 2003.
- [28] C. Gilliam, P. L. Dragotti, and M. Brookes, "On the spectrum of the plenoptic function," *IEEE Transactions on Image Processing*, vol. 23, no. 2, pp. 502-516, 2013.
- [29] Q. Zhao, F. Dai, J. Lv, Y. Ma, and Y. Zhang, "Panoramic light field from hand-held video and its sampling for real-time rendering," *IEEE Transactions on Circuits and Systems for Video Technology*, vol. 30, no. 4, pp. 1011-1021, 2019.
- [30] B. T. Phong, "Illumination for computer generated pictures," *Communications of the ACM*, vol. 18, no. 6, pp. 311-317, 1975.
- [31] S. G. Narasimhan and S. K. Nayar, "Shedding light on the weather," in *IEEE Computer Society Conference on Computer Vision and Pattern Recognition*, 2003, vol. 1: IEEE, pp. 1-8.
- [32] S. Metari and F. Deschenes, "A new convolution kernel for atmospheric point spread function applied to computer vision," in *IEEE 11th international conference on computer vision*, 2007: IEEE, pp. 1-8.
- [33] R. Wang, R. Li, and H. Sun, "Haze removal based on multiple scattering model with superpixel algorithm," *Signal Processing*, vol. 127, pp. 24-36, 2016.
- [34] R. N. Mahalati and J. M. Kahn, "Effect of fog on free-space optical links employing imaging receivers," *Optics Express*, vol. 20, no. 2, pp. 1649-1661, 2012.
- [35] S. Chandrasekhar, *Radiative Transfer*. New York: Dover Publications Inc, 1960.
- [36] A. Ishimaru, *Wave propagation and scattering in random media*. New York: Academic press, 1978.
- [37] Y. Yuan, "Recent advances in trust region algorithms," *Mathematical Programming*, vol. 151, no. 1, pp. 249-281, 2015.
- [38] D. F. Swinehart, "The beer-lambert law," *Journal of chemical education*, vol. 39, no. 7, pp. 333-335, 1962.
- [39] Z. Deng, D. Ji, L. Gu, M. Sun, and X. Yao, "Underwater Image Enhancement Algorithm Adapted to Different Turbidities Ranges," in *2018 IEEE 8th International Conference on Underwater System Technology: Theory and Applications (USYS)*, 2018: IEEE, pp. 1-6.
- [40] C. Tang, R. Sun, Z. Lian, and W. Zhu, "PLSMS model for restoration of the details concealed by light sources in nighttime hazed image," *Signal, Image and Video Processing*, vol. 15, pp. 411-419, 2021.
- [41] H. Zhang, Q. Dan, and L. Wang, "From Point to Surface: Realistic and Perceptually-Plausible Hazy Image Generation with Glow-Diffusion," in *Chinese Conference on Pattern Recognition and Computer Vision (PRCV)*, 2024: Springer, pp. 89-102.
- [42] J. Benesty, J. Chen, Y. Huang, and I. Cohen, "Pearson correlation coefficient," in *Noise reduction in speech processing*: Springer, 2009, pp. 1-4.
- [43] J. F. Kenney and E. Keeping, "Root mean square," *Mathematics of statistics*, vol. 1, pp. 59-60, 1962.
- [44] C. J. Willmott and K. Matsuura, "Advantages of the mean absolute error (MAE) over the root mean square error (RMSE) in assessing average model performance," *Climate research*, vol. 30, no. 1, pp. 79-82, 2005.
- [45] R. Bracewell, "Pentagram notation for cross correlation. The Fourier transform and its applications," *New York: McGraw-Hill*, vol. 46, p. 243, 1965.
- [46] Z. Wang, A. C. Bovik, H. R. Sheikh, and E. P. Simoncelli, "Image quality assessment: from error visibility to structural similarity," *IEEE transactions on image processing*, vol. 13, no. 4, pp. 600-612, 2004.
- [47] Z. Wei *et al.*, "De-scattering deep neural network enables fast imaging of spines through scattering media by temporal focusing microscopy," *Research Square*, 2023.
- [48] *Specifications for surface meteorological observation— Meteorological visibility*, 2017.
- [49] X. Min, G. Zhai, K. Gu, X. Yang, and X. Guan, "Objective quality evaluation of dehazed images," *IEEE Transactions on Intelligent Transportation Systems*, vol. 20, no. 8, pp. 2879-2892, 2018.
- [50] Y. Lee and H. Yoo, "Three-dimensional visualization of objects in scattering medium using integral imaging and spectral analysis," *Optics and Lasers in Engineering*, vol. 77, pp. 31-38, 2016.



Yihui Fan is currently working toward the Ph.D. degree in the Control Science and Engineering with Shenzhen International Graduate School, Tsinghua University, China. His research interests include the development of new systems and algorithms for solving problems in light field sampling theory scattering imaging and light-field image stitching. He has published paper in IEEE TCSVT. He was the recipient of the Gold Medal of International Exhibition of Inventions of Geneva in 2024 and CITA Best Oral Presentation Award in 2023.



Dongyu Du received the Ph.D. degree in the Control Science and Engineering at Tsinghua University Automation Department, China. Her research interests include the development of new systems and algorithms for solving problems in scattering imaging, non-line-of-sight imaging and single-photon imaging.



Hongkun Cao received the Ph. D. degree in electronics engineering from Kwangwoon University, Seoul, South Korea, in 2020. From 2020-2022, he was a Postdoctoral Fellow with the Shenzhen International Graduate School, Tsinghua University. Since 2022, he has been with Pengcheng Laboratory, where he is a research associate. His current research interests include 3D display, holography, computational imaging. He was awarded as Shenzhen Overseas High-level Talents (Category C) in 2020.



Jiayu Xie received the M.E. degree with Shenzhen International Graduate School, Tsinghua University. His research interests focus on multimodal image registration and image dehazing.



Xin Jin (Senior Member, IEEE) received the M.S. degree in communication and information system and the Ph.D. degree in information and communication engineering from the Huazhong University of Science and Technology, Wuhan, China, in 2002 and 2005, respectively. From 2006 to 2008, she was a Postdoctoral Fellow with The Chinese University of Hong Kong, Hong Kong. From 2008 to 2012, she was a Visiting Lecturer with Waseda University, Fukuoka, Japan. Since March 2012, she has been with Shenzhen International Graduate School, Tsinghua University, Beijing, China, where she is currently a Professor. She has authored or coauthored more than 200 conference and journal papers. Her research interests include computational imaging and power-constrained video processing and compression. She is also the Distinguished Professor of Pengcheng Scholar. She was the recipient of the Gold Medal of International Exhibition of Inventions of Geneva in 2024 and 2022, the Second Prize of National Science and Technology Progress Award in 2016, first Prize of Guangdong Science and Technology Award in 2015, and ISOC Best Paper Award in 2010. Dr. Jin is the Senior Member of IEEE, Member of SPIE and ACM.